

## Characterization and light-induced dynamics of alkanethiol-capped gold nanoparticles supracrystals by small-angle ultrafast electron diffraction

**Authors:** Giulia Fulvia Mancini<sup>1\*</sup>, Tatiana Latychevskaia<sup>2</sup>, Francesco Pennacchio<sup>1</sup>, Javier Reguera<sup>3,†,‡</sup>, Francesco Stellacci<sup>3</sup> & Fabrizio Carbone<sup>1</sup>

### Affiliations:

<sup>1</sup>Laboratory for Ultrafast Microscopy and Electron Scattering, Institute of Condensed Matter Physics, École Polytechnique Fédérale de Lausanne, CH-1015 Lausanne, Switzerland.

<sup>2</sup>Physics Institute, University of Zurich, Winterthurerstrasse 190, 8057 Zurich, Switzerland.

<sup>3</sup>Supramolecular Nanomaterials and Interfaces Laboratory, Institute of Materials, École Polytechnique Fédérale de Lausanne, CH-1015 Lausanne, Switzerland.

Correspondence and requests for materials should be addressed to F. Carbone (fabrizio.carbone@epfl.ch).

Present address:

<sup>†</sup> CIC biomaGUNE, Paseo de Miramón 182C, 20009 Donostia-San Sebastian, Spain.

<sup>‡</sup> Ikerbasque, Basque Foundation for Science, 48011 Bilbao, Spain.

**Metal nanoparticles (NPs) are promising candidates for applications from electronics to medicine<sup>1-3</sup>. Their metallic core provides some key properties, *e.g.* magnetization, plasmonic response or conductivity, with the ligand molecules providing others like solubility, assembly or interaction with biomolecules<sup>4, 5</sup>. Even more properties can be engineered when these NPs are used as building blocks to form supracrystals<sup>2, 6-7</sup>. The formation of these supracrystals depends upon a complex interplay between many forces, some stemming from the core, some from the ligand<sup>8</sup>. At present, there is no known approach to characterize the local order of ligand molecules in such complex supracrystals or their dynamics, with a spatial resolution ranging from the NPs cores and their ligands, to the larger scale domains arrangement. Here, we develop a methodology based on small-angle ultrafast electron diffraction to characterize different two-dimensional supracrystals of alkanethiol-coated gold nanoparticles with femtosecond time, sub-nanometer spatial resolution and sensitivity down to the carbon and hydrogen atoms in the ligands. We retrieve the static arrangement of the ligands in different supracrystals and show that both disordering and ordering dynamics can be achieved upon ultrafast laser excitation, demonstrating that nanoparticles self-organization can be triggered by light. We anticipate that this methodology will enable the systematic investigation of the dynamical structural properties of nano-assembled materials, in particular those composed of light elements relevant for biological applications.**

Ultrafast Electron Diffraction (UED) and X-ray diffraction (XRD) delivered microscopic information on the structural dynamics of non-functionalized polycrystalline gold thin films<sup>9-12</sup>, isolated NPs<sup>13</sup> and gold NPs suspended on organic membranes<sup>14</sup>. All these experiments were limited at the observation of the intra-NP dynamics, and none dealt with functionalized NPs. With respect to X-rays, electrons offer a higher sensitivity in thin samples containing light elements<sup>15, 16</sup> at the cost of the transverse coherence<sup>17</sup>. Coherent small-angle femtosecond (fs)-electron diffraction experiments presented in this work can access the length-scale between few Ångstrom (Å) to a few nanometers (nm) with fs time-resolution and sensitivity to the organic ligands. To do this, a trade-off between the beam brightness and its coherence at the sample was found in our high-flux ( $10^9$  e<sup>-</sup>/sec) UED set-up<sup>18</sup>.

Samples of 1-octanethiol-coated, 1-dodecanethiol-coated, and 1-octadecanethiol-coated gold NPs were prepared for transmission electron diffraction experiments<sup>19</sup>. A Transmission Electron Microscopy (TEM) image of the 1-dodecanthiol-coated NPs supracrystal, characterized by an average NPs core diameter of 5.70 nm and a polydispersity of 9%, is shown in Fig. 1a with its crystallographic planes. A beam of fs optical pulses was used to generate both the probing electrons (30 keV,  $\lambda=7$  pm) and the photo-excitation. Fs snapshots of the diffraction pattern from the NPs supracrystal were recorded at different time-delays between the pump photo-excitation and the probe, building a fs-resolved movie of the dynamics of the sample. Photoinduced changes were initiated by 1.5 eV, 50 fs pulses at an absorbed fluence of  $100 \mu\text{J}/\text{cm}^2$  (18, 19). The size of the beam and the sample-to-camera distance were optimized so that the transverse coherence was comparable to the distances of interest in the sample ( $\sim 10$  nm), corresponding to small deflection angles in the mrad range. Such a condition allows the observation of the speckle pattern originating from the constructive and destructive interference of the scattered wave from the supracrystal periodicities.

The diffraction pattern of the 1-dodecanthiol-coated sample at equilibrium depicted in Fig. 1b is the result of the stitching of two different experimental diffraction patterns. The separation between the two contributing diffraction patterns is marked by the black line at  $s=2.38 \text{ Å}^{-1}$ . One diffraction pattern was recorded with a beam-block covering the direct electron beam up to a scattering vector value  $s=2.38 \text{ Å}^{-1}$  to enhance the high-order diffraction from the NPs gold cores. The other diffraction pattern was acquired without beam stop and it spans the scattering vectors from  $s=0 \text{ Å}^{-1}$  to  $s=2.38 \text{ Å}^{-1}$  thus exhibiting the “small-angle” diffraction region. Figure 1c displays the two-dimensional Fourier Transform (FT) of the TEM image of the 1-dodecanthiol-coated sample, covering the scattering vector range up to a value of  $0.39 \text{ Å}^{-1}$ . Figure 1d displays the simulated diffraction pattern obtained by the Superposition of Atomic Scattering Amplitudes (SASA) from individual atoms in the NPs, where the geometrical arrangement of the NPs in the supracrystal is deduced from the TEM image of the sample (Fig. 1a), and the shape of the NPs and the orientation of the ligands on their surface are modeled according to previous reports<sup>19-22</sup>. The detailed description of the SASA simulation is addressed in the supplementary text. The

diffraction patterns of Fig. 1b and Fig. 1d are reported on the same scale ( $s=0$  to  $s=5.98 \text{ \AA}^{-1}$ ) to allow a direct comparison of the diffraction features. The radial averaged intensity of the typical Debye-Scherrer rings from polycrystalline gold is reported in Fig. 2 (violet circles) and gives the characteristics distances of the face-centered-cubic (*fcc*) motif of gold, with  $a=4.08 \text{ \AA}$  and  $\text{Au}_{(111)}=2.35 \text{ \AA}$ , showing consistency with the result of the SASA simulation of the gold cores (orange solid line in Fig. 2). In Fig. 2, the comparison between the experimental electron diffraction and the FT of the TEM image is depicted in the scattering vectors range from  $s=0 \text{ \AA}^{-1}$  to  $s=0.39 \text{ \AA}^{-1}$ ; at higher scattering vectors, the comparison is carried out between the experimental diffraction pattern and the SASA simulation. A detailed investigation of the peaks indicated in Fig. 2 is presented below.

To study the azimuthal dependence of the speckle intensity at a specific scattering vector  $s$ , we introduce the Angular Normalized Intensity (ANI):

$$\text{ANI}(s, \theta) = \frac{I(s, \theta) - I(s)}{I(s)} \quad (1)$$

where  $I(s)$  is the radial averaged intensity at  $s$ , corresponding to a specific real-space distance. Modulations in ANIs are observed both in the experimental and the simulated patterns, revealing specific symmetries in the NPs supracrystal. These modulations are characterized by a folding, *i.e.* the number of maxima over  $2\pi$ , which is determined by the symmetry of the real-space object within the sample. The ANI curves at specific  $s$  feature a distribution that can be fitted with a harmonic function providing a guide to the eye for the ANI folding. In our experiment six different regions of scattering vectors  $s$  were determined, each with a specific ANI folding and defined by a precise range of scattering vectors  $[s(i), s(i)+\Delta s]$ ,  $i = 1 \dots 6$ . Within each region the ANI folding is preserved and its amplitude is maximum at the region center ( $\text{ANI}_{\max}(s, \theta)$ ), as reported in Table 1. The distribution of the ANI amplitude within a single region was assigned through the computation of the contrast ( $C(s)$ ):

$$C(s) = -\left\langle \left| (\text{ANI}_{\max}(s, \theta) - \text{ANI}(s, \theta)) \right|^2 \right\rangle_{\theta} \quad \text{with } s \in [s(i), s(i)+\Delta s], \quad (2)$$

where  $\text{ANI}(s, \theta)$  is the ANI at every  $s$  within the selected region  $[s(i), s(i)+\Delta s]$ ,  $\text{ANI}_{\max}(s, \theta)$  is the maximum amplitude within the same region, and  $\langle \rangle_{\theta}$  denotes averaging over  $\theta$ . The contrast  $C(s)$  changes as a function of  $s$ , showing six different contrast peaks, reported in Fig. 2 (blue circles) along with the indication of the distances in real space that correspond to the characteristic lengths of the sample (summarized in Table 1). Peaks  $C_1$  and  $C_2$  are families of different overlapping peaks, as identified by comparison with the FT of the TEM image; peaks  $C_3$ ,  $C_4$ ,  $C_5$  and  $C_6$  can be attributed to distinct scattering features.

Local symmetries are also retrieved through high-order correlations in the angular distribution of the speckles from the NPs supracrystal, following the calculation of the diagonalized 2-point Cross Correlation Function (CCF) defined as<sup>23, 24</sup>:

$$C_s(\Delta) = \frac{\langle I(s, \theta)I(s, \theta + \Delta) \rangle_\theta - \langle I(s, \theta) \rangle_\theta^2}{\langle I(s, \theta) \rangle_\theta^2} \quad (3)$$

where  $I(s, \theta)$  represents the scattered intensity at defined scattering vector value  $s$ , and azimuthal angle  $\theta$ , while  $\Delta$  is the shift between two azimuthal angles. The  $\langle \rangle_\theta$  denotes averaging over  $\theta$ . The details on the formalism of the angular cross-correlation analysis are reported elsewhere<sup>25, 26</sup>.

The low-order peaks are attributed to the arrangement of the NPs in the supracrystal. To mimic their distribution we used the several Sphere Lattice Model (SLM) simulations, where each NP is represented by a sphere<sup>21</sup>. The results from two SLM models are shown in Fig. 3(a-c) for different disordering conditions, yielding the best agreement with the experiments for a sphere diameter of 5.70 nm, and a closed-packing arrangement with a core-to-core distance of 7.63 nm. These parameters give the distance  $d_0=6.61$  nm between the planes of crystallographically arranged NPs in the supracrystal (upper inset of Fig. 1a). Figure 3c shows that the peak  $s_{0,3}$  is narrow in the case of ideally ordered NPs (green trace), and is broadened and less intense upon NPs disordering (yellow), consistently with the FT of the TEM image of the sample (purple). In Fig. 2, the experimental contrast peaks  $C_1$  and  $C_2$  are compared to the radial averaged intensity profile obtained from the FT of the TEM image (purple solid line). The diffraction at  $s_{0,1}$  (first order of  $d_0$ ) is overexposed by the central beam, while the higher diffraction orders of  $d_0$  ( $s_{0,n} = n \cdot \frac{2\pi}{d_0}$  with  $n=2^{\text{nd}}, 3^{\text{rd}}, 4^{\text{th}}$  order), are detected both in the experimental diffraction and in

the FT of the TEM image. The contrast peak  $C_2$  ( $s=0.25\text{--}0.40 \text{ \AA}^{-1}$ ) is a superposition of  $s_{0,3}=0.28 \text{ \AA}^{-1}$  and  $s_{0,4}=0.38 \text{ \AA}^{-1}$ , which represent respectively the third and fourth order of diffraction from the crystallographic planes with spacing  $d_0$ . Figure 3d shows the  $C_s(s=s_{0,3}, \Delta)$  curves obtained from three different images: the experimental electron diffraction (blue curve), the FT of the TEM image (red curve) and the FT of the SLM simulation in Fig. 3b (orange curve). The three  $C_s(\Delta)$  curves show a six-fold symmetry, which is consistent with the hexagonal geometry of the two-dimensional supracrystal.

The contrast peaks  $C_4$  and  $C_5$  correspond to the distances ranging from the NPs ligand-to-ligand to the atomic ones. For these short distances (see Table 1) the atomic arrangement of gold cores and ligands is more relevant to the analysis of the speckle pattern than the two-dimensional distribution of NPs in the supracrystal, modeled with the SLM simulations. For this reason the speckle features at  $C_4$  and  $C_5$  are assigned by comparison with the SASA simulated diffraction pattern, as shown in Fig. 2. The  $C_s(\Delta)$  at  $s_4$  is reported in Fig. 3e; the related curve obtained from

the SASA simulated diffraction pattern exhibits six maxima and thus reflects the hexagonal symmetry of the superlattice with which the dodecanethiol ligands bind to the Au<sub>(111)</sub> facets of the NP core, and whose real-space distance  $d_4 = 4.98 \text{ \AA}$  corresponds to the ligand-ligand spacing, rendered in Fig. 3h. The experimental electron diffraction pattern at  $s_4$  yields a six-fold  $C_s(\Delta)$  profile (blue curve, Fig. 3e). The same methodology, based on the computation of  $C_s(\Delta)$  at  $s_4$ , has been applied to determine the local atomic arrangement of the ligand chains on the NPs surface in supracrystals of 1-octanethiol and 1-octadecanethiol-capped gold NPs. As for the 1-dodecanethiol-capped gold NPs, the alkanethiol molecules arrange in the zig-zag *trans* configuration on the facets of the NPs core leading to the interdigitation of molecular bundles on neighboring particles<sup>19</sup>. Ligands partially interdigitate among neighboring NPs to compensate for the loss of density at the terminal part of the chains; a minority of *gauche* chains occupy interstitial sites and domain boundaries<sup>19, 21, 22</sup>. Longer ligand chains (number of Carbon atoms  $n_C > 8$ ) are known to be more thermodynamically stable as zig-zag *trans* isomers due to the chain-chain interaction of the van der Waals and dipole-dipole kind. Thus, for systems with  $n_C > 8$  the higher degree of local order is reflected by the presence of a superlattice at  $s_4$ . In our system, this is detected directly in the speckle pattern from each sample, and the presence of the superlattice ordering at  $s_4$  is unraveled by the angular cross-correlation analysis. In Fig. 3f evidence for the hexagonal arrangement has been found in the six-fold  $C_s(\Delta)$  profile of the 1-dodecanethiol (blue circles) and of the 1-octadecanethiol-capped gold NPs (violet rhombuses), while no local ordering has been determined for 1-octanethiol-capped gold NPs, as expected (green squares). This systematic investigation of different samples shows the robustness of our crystallographic assignments.

For the 1-dodecanethiol-capped gold NPs supracrystal the  $C_s(\Delta)$  at  $s_5$  is four-fold in both the experimental and simulated diffraction patterns, as shown in Fig. 3g. This periodicity results from the superposition of two different two-fold centro-symmetrical diffraction patterns created by the carbon atoms of the ligands which align on the NPs facets according to preferential orientations (Fig. 3i). This is demonstrated in the dedicated simulation reported in the supplementary information.

Next, we studied the behavior of the 1-dodecanethiol-capped gold NPs supracrystal under photoexcitation. The time evolution of the amplitude and position of the contrast peaks gives information on the photo-induced changes of the associated real-space features of the sample. The temporal evolution of the peak  $C_2$ , related to the family of crystallographic planes depicted in the upper inset of Fig. 1a, shows an exponential decay of the intensity with a time constant of  $11 \pm 3 \text{ ps}$  and no changes in its position (Fig. 4, a and b-red squares). The decay of intensity is an evidence for the photo-induced disorder of the NPs in the supracrystal. The light pulse also induces a dynamics in the ligands connecting NPs *via* both interdigitation and interlocking of molecular bundles. The temporal evolution of  $C_4$ , associated to the superlattice of S atoms, shows no changes in the scattering vector position within our experimental accuracy (Fig. 4b). A

significant increase of the  $C_4$  peak intensity is observed instead (Fig. 4d), with a time scale of  $30 \pm 4$  ps obtained by mono-exponential fit, manifesting a clear tendency of the ligands to order themselves throughout the sample. This scenario is also confirmed by the temporal behavior of the contrast peak  $C_5$ , associated with the arrangement of carbon atoms. The intensity of  $C_5$  is also found to increase upon photo-excitation with a similar time-scale as  $C_4$  (Fig. 4c). Thus, one can conclude that the relatively well arranged ligand molecules on the facets of every NP in the supracrystal show the tendency to increase their degree of alignment upon photo-excitation. This experimental observation is consistent with the evidence of a tens of ps “ultrafast annealing” in a self-assembled monolayer of 2-mercaptoacetic acid molecules adsorbed on single-crystal clean  $\text{Au}_{(111)}$  surfaces, investigated by means of UED<sup>27</sup>. The time dependence of the intensity associated with the reflections from the  $\text{Au}_{(311)}$  planes is depicted in Fig. 4a (blue rhombuses) and it exhibits an exponential decay with time constant of  $18 \pm 3$  ps, signaling an increased disorder of the crystalline cores.

Photo-excitation causes thermal disorder in both the gold cores ( $18 \pm 3$  ps) and the supracrystal ( $11 \pm 3$  ps). As a result, the supracrystal local triangular lattice arrangement is perturbed. Since bundles of ligands interdigitate and interlock between neighboring NPs, the motion of the NPs causes a stretching of the ligands. This motion takes place with a slower dynamics ( $30 \pm 4$  ps) and leads to a more ordered arrangement of the ligands throughout the probed sample area. The recovery time for the re-arranged system is beyond the probed time-scale range, *i.e.* 220 ps after light exposure. This dynamics is represented in a computer-simulated movie (see Extended Data Movie S1) from which two frames, one before and one after  $t_0$ , are reported in Fig. 4(e, f).

In disordered elastic media, elastic forces of different origin, chemical, magnetic or electrostatic, provide the binding necessary to create order<sup>28</sup>. Their interplay with disorder, of thermal or quantum origin, gives rise to universal behaviours whose investigation has been mostly limited to the observation of frozen systems close to equilibrium<sup>29, 30</sup>. However, ordering and disordering phenomena are essentially dynamical. In our study, we demonstrate that it is now possible to obtain movies of the interplay between disorder and elastic forces with a spatial resolution that allows distinguishing every microscopic constituent of the system and a temporal resolution in the time scale of their motions.

## References and Notes:

1. Nakanishi, H. *et al.* Dynamic internal gradients control and direct electric currents within nanostructured materials. *Nat. Nanotechnol.* **6**, 740–746 (2011).
2. Kim, Y. *et al.*, Stretchable nanoparticle conductors with self-organized conductive pathways. *Nature* **500**, 59–63 (2013).
3. De, M., Ghosh, P. S. & Rotello, V. M. Applications of nanoparticles in biology. *Adv. Mater.* **20**, 4225–4241 (2008).
4. Feldheim, D. L. & Foss, C. A., Jr. *Metal nanoparticles, synthesis, characterization and applications* (CRC Press, 2001).
5. Schmid, G. *Nanoparticles: from theory to application* (Wiley-VCH, 2006).
6. Pileni, M.-P. Self-assembly of inorganic nanocrystals: fabrication and collective intrinsic properties. *Acc. Chem. Res.* **40**, 685–693 (2007).
7. Talapin, D. V., Lee, J.-S., Kovalenko, M. V. & Shevchenko, E. V. Prospects of colloidal nanocrystals for electronic and optoelectronic applications. *Chem. Rev.* **110**, 389–458 (2010).
8. Bishop, K. J. M., Wilmer, C. E., Soh, S. & Grzybowski, B. A. Nanoscale forces and their uses in self-Assembly. *Small* **5**, 1600–1630 (2009).
9. Schäfer, S., Liang, W. & Zewail, A. H. Structural dynamics of nanoscale gold by ultrafast electron crystallography. *Chem. Phys. Lett.* **515**, 278–282 (2011).
10. Ernstorfer, R. *et al.*, The formation of warm dense matter: experimental evidence for electronic bond hardening in gold. *Science* **323**, 1033–1037 (2009).
11. Chen, J., Chen, W.-K., Tang, J. & Rentzepis, P. M. Time-resolved structural dynamics of thin metal films heated with femtosecond optical pulses. *Proc. Natl. Acad. Sci. U. S. A.* **108**, 18887–18892 (2011).
12. Chen, J., Chen, W.-K. & Rentzepis, P. M. Blast wave and contraction in Au(111) thin film induced by femtosecond laser pulses. A time resolved x-ray diffraction study. *J. Appl. Phys.* **109**, 113522 (2011).
13. Clark, J. N. *et al.*, Ultrafast three-dimensional imaging of lattice dynamics in individual gold nanocrystals. *Science* **341**, 56–59 (2013).
14. Ruan, C.-Y., Murooka, Y., Raman, R. K. & Murdick, R. A. Dynamics of size-selected gold nanoparticles studied by ultrafast electron nanocrystallography. *Nano Lett.* **7**, 1290–1296 (2007).
15. Carbone, F., Musumeci, P., Luiten, O. J. & Hebert, C. A perspective on novel sources of ultrashort electron and X-ray pulses. *Chem. Phys.* **392**, 1–9 (2012).
16. Piazza, L., Musumeci, P., Luiten, O. J. & Carbone, F. A proposal for fs-electron microscopy experiments on high-energy excitations in solids. *Micron* **63**, 40–46 (2014).

17. Spence, J. C. H., Weierstall, U. & Howells, M. Coherence and sampling requirements for diffractive imaging. *Ultramicroscopy* **101**, 149–152 (2004).
18. Mancini, G. F. *et al.* Design and implementation of a flexible beamline for fs electron diffraction experiments. *Nucl. Instrum. Methods Phys. Res. A* **691**, 113-122 (2012).
19. Materials and methods are available in the supplementary information.
20. Whetten, R. L. *et al.* Nanocrystal gold molecules. *Adv. Mater.* **8**, 428-433 (1996).
21. Badia, A. *et al.* Self-Assembled Monolayers on Gold Nanoparticles. *Chem. Eur. J.* **2**, 359-363 (1996).
22. Badia, A., Cuccia, L., Demers, L., Morin, F. & Lennox, R. B. Structure and dynamics in alkanethiolate monolayers self-assembled on gold nanoparticles: A DSC, FT-IR, and deuterium NMR study. *J. Am. Chem. Soc.* **119**, 2682-2692 (1997).
23. Wochner, P. *et al.* X-ray cross correlation analysis uncovers hidden local symmetries in disordered matter. *Proc. Natl. Acad. Sci. U. S. A.* **106**, 11511-11514 (2009).
24. Wochner, P., Castro-Colin, M., Bogle, S. N. & Bugaev, V. N. Of fluctuations and cross-correlations: finding order in disorder. *Int. J. Mat. Res.* **102**, 874-888 (2011).
25. Altarelli, M., Kurta, R. P. & Vartanyants, I. A. X-ray cross-correlation analysis and local symmetries of disordered systems: General theory. *Phys. Rev. B* **82**, 104207 (2010).
26. Kurta, R., Altarelli, M., Weckert, E., Vartanyants I. A., X-ray cross-correlation analysis applied to disordered two-dimensional systems. *Phys. Rev. B* **85**, 184204 (2012).
27. Ruan, C.-Y., Yang, D.-S. & Zewail, A. H. Structures and dynamics of self-assembled surface monolayers observed by ultrafast electron crystallography. *J. Am. Chem. Soc.* **126**, 12797-12799 (2004).
28. Giamarchi, T. in *Encyclopedia of Complexity and Systems Science*, (Springer, 2009), pp. 2019-2038.
29. Giamarchi, T. & Le Doussal, P. Elastic theory of flux lattices in the presence of weak disorder. *Phys. Rev. B* **52**, 1242-1270 (1995).
30. Klein, T. *et al.* A Bragg glass phase in the vortex lattice of a type II superconductor. *Nature* **413**, 404-406 (2001).
31. Ong, Q. K. *et al.* High-resolution scanning tunneling microscopy characterization of mixed monolayer protected gold nanoparticles. *ACS Nano* **7**, 8529–8539 (2013).
32. Zheng, N. Fan, J. & Stucky, G. D. One-step one-phase synthesis of monodisperse noble-metallic nanoparticles and their colloidal crystals. *J. Am. Chem. Soc.* **128**, 6550-6551 (2006).
33. Lee, Z. *et al.* Direct imaging of soft–hard interfaces enabled by graphene. *Nano Lett.* **9**, 3365–3369 (2009).



34. Panthani, M. G. *et al.* Graphene-supported high-resolution TEM and STEM imaging of silicon nanocrystals and their capping ligands. *J. Phys. Chem. C* **116**, 22463–22468 (2012).
35. van Oudheusden, T. *et al.* Compression of subrelativistic space-charge-dominated electron bunches for single-shot femtosecond electron diffraction. *Phys. Rev. Lett.* **105**, 264801 (2010).
36. Kiewiet, F. B., Kemper, A. H., Luiten, O. J., Brussaard, G. J. H., van der Wiel, M. J. Femtosecond synchronization of a 3 GHz RF oscillator to a mode-locked Ti:sapphire laser. *Nucl. Instrum. Methods Phys. Res. A* **484**, 619–624 (2002).
37. Wang, Y., Teitel, S. & Dellago, C. Melting and equilibrium shape of icosahedral gold nanoparticles. *Chem. Phys. Lett.* **394**, 257–261 (2004).
38. Wang, Y., Teitel, S. & Dellago, C. Melting of icosahedral gold nanoclusters from molecular dynamics simulations. *J. Chem. Phys.* **122**, 214722 (2005).
39. Daniel, M.-C. & Astruc, D. Gold nanoparticles: assembly, supramolecular chemistry, quantum-size-related properties, and applications toward biology, catalysis, and nanotechnology. *Chem. Rev.* **104**, 293 (2004).
40. Damasceno, P. F., Engel, M. & Glotzer, S. C. Predictive self-assembly of polyhedra into complex structures. *Science* **337**, 453 (2012).
41. Badia, A., Lennox, R. B. & Reven, L. A dynamic view of self-assembled monolayers. *Acc. Chem. Res.* **33**, 475–481 (2000).
42. Terrill, R. H. *et al.* Monolayers in three dimensions: NMR, SAXS, thermal, and electron hopping studies of alkanethiol stabilized gold clusters. *J. Am. Chem. Soc.* **117**, 12537–12548 (1995).
43. Vericat, C., Vela, M. E. & Salvarezza, R. C. Self-assembled monolayers of alkanethiols on Au(111): surface structures, defects and dynamics. *Phys. Chem. Chem. Phys.* **7**, 3258–3268 (2005).
44. Schreiber, F. Structure and growth of self-assembling monolayers. *Prog. Surf. Sci.* **65**, 151–256 (2000).
45. Zanchet, D., Tolentino, H., Martins Alves, M. C., Alves, O. L. & Ugarte, D. Inter-atomic distance contraction in thiol-passivated gold nanoparticles *Chem. Phys. Lett.* **323**, 167–172 (2000).
46. Treacy, M. M. J., Gibson, J. M., Fan, L., Paterson, D. J. & McNulty, I. Fluctuation microscopy: a probe of medium range order. *Rep. Prog. Phys.* **68**, 2899–2944 (2005).

**Acknowledgements:** The experimental work was funded by the Swiss National Science Foundation (SNSF) through the grant No. PP00P2–128269/1. The authors acknowledge B. Patterson, B. Mansart and A. Al Haddad for useful discussions.

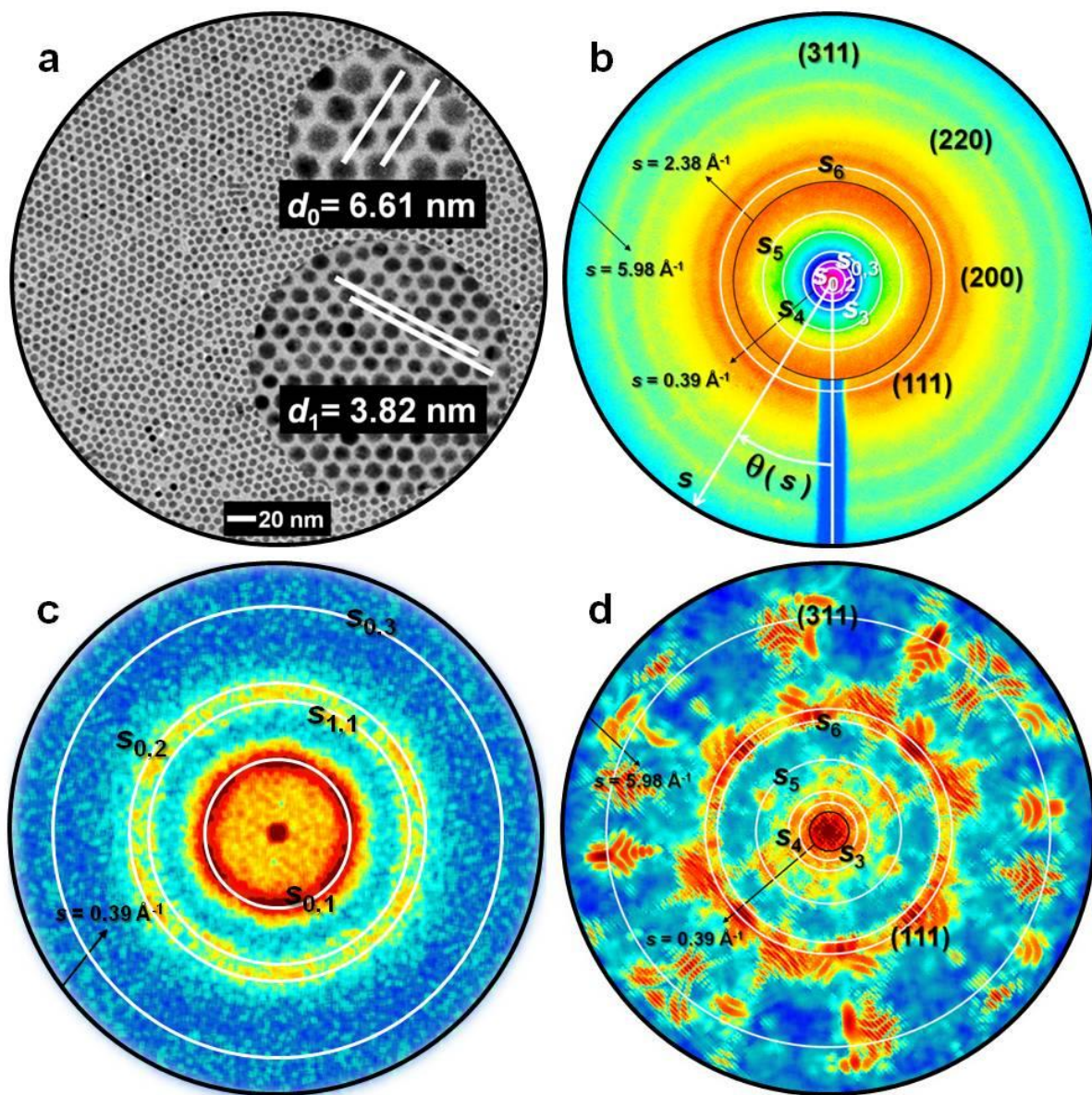


**Fig. 1. Static small-angle electron diffraction.** **a)** TEM image of the sample. Insets: arrangement of the NPs and crystallographic planes with distances  $d_0$  and  $d_1$ . **b)** Experimental diffraction pattern given by the stitching of the large-angle and small-angle regions<sup>19</sup>. **c)** FT of the TEM image. **d)** Simulated diffraction pattern by Superposition of Atomic Scattering Amplitudes (SASA) from individual atoms in the NPs.

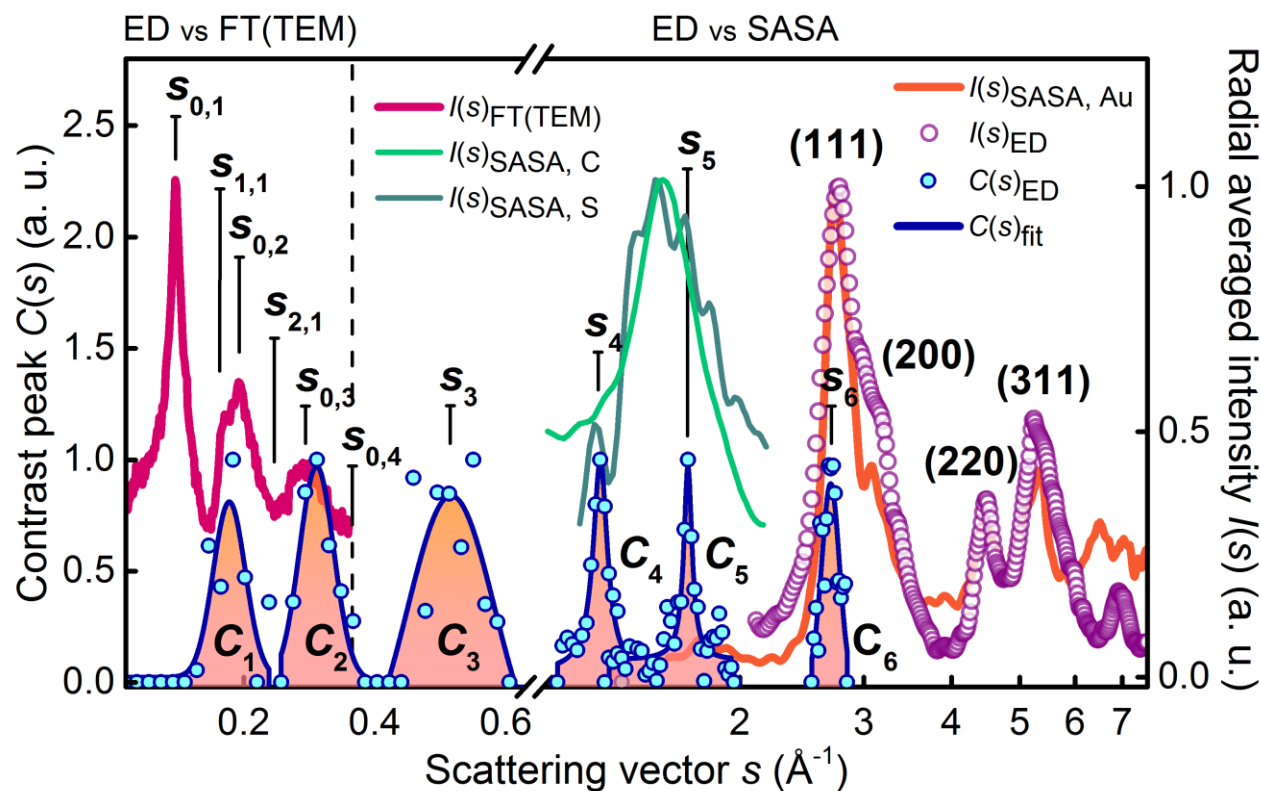


**Fig. 2. Contrast peaks and radial averaged intensity peaks.** The dependence of  $C(s)$  on the scattering vector is plotted with blue circles (see Table 1). Each peak is fitted to a Lorentzian function (blue solid line). The contrast peaks  $C_1$  and  $C_2$  are compared to the radial averaged intensity of the FT of the TEM image (purple solid line). The different diffraction peaks are labeled from the first orders of  $d_0$  ( $s_{0,1}$ ),  $d_1$  ( $s_{1,1}$ ) and  $d_2$  ( $s_{2,1}$ ). The contrast peaks  $C_4$  and  $C_5$  are compared to the radial averaged intensity of the SASA simulation carried out taking into account the scattering functions of Sulfur (dark green) and Carbon (light green) atomic elements in the cluster. At higher scattering vectors the radial averaged intensity from the experiments (violet circles) and from the SASA simulation of the NPs gold cores (orange solid line) are plotted together for comparison.



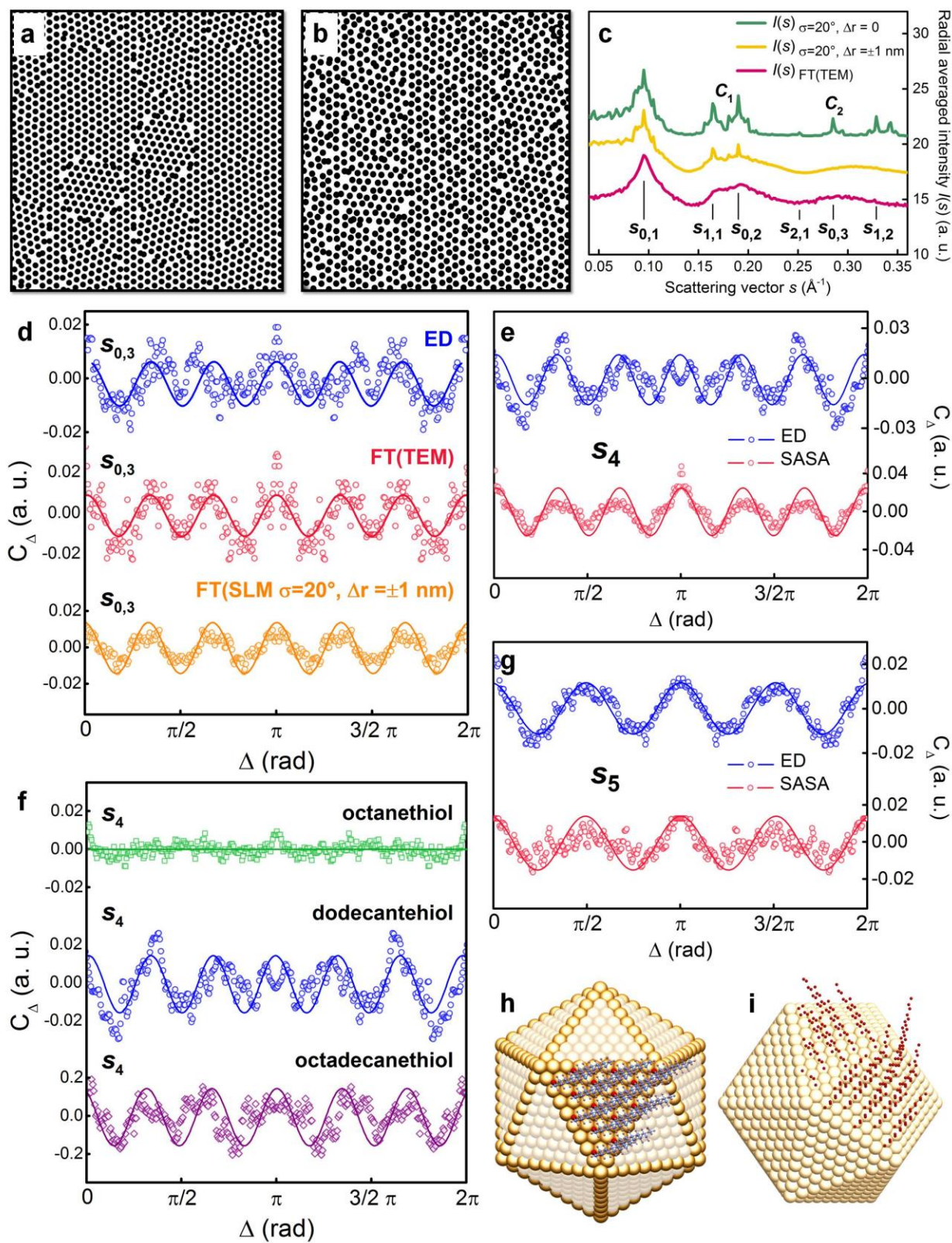


**Fig. 3. NPs and ligands distributions at equilibrium.** **a)** NPs distribution simulated in SLM (domains rotation  $\sigma = 20^\circ$ , NPs displacement  $\Delta r = 0$ ). **b)** SLM simulation with  $\sigma = 20^\circ$ ,  $\Delta r = \pm 1$  nm. **c)** Radial averaged intensity  $I(s)$  of the two SLM simulations. The green profile is obtained from the FT of the SLM ( $\sigma = 20^\circ$ ,  $\Delta r = 0$ ), and the yellow one from the SLM ( $\sigma = 20^\circ$ ,  $\Delta r = \pm 1$  nm). The radial averaged intensity from the experimental FT of the TEM image is shown in purple. **d)** Comparison of the  $C_s(\Delta)$  at  $s_{0,3}$  in the experimental diffraction pattern (blue), the FT of the TEM image (red) and in the FT of the SLM ( $\sigma=20^\circ, \Delta r = \pm 1$  nm) (orange profile). **e)**  $C_s(\Delta)$  at  $s_4$  from both the experimental (blue) and SASA (red) simulated diffraction patterns. **f)**  $C_s(\Delta)$  at  $s_4$  for 1-octanethiol (green squares), 1-dodecanethiol (blue circles) and 1-octadecanethiol-capped gold NPs (violet rhombuses) evidencing local order for the samples with  $n_C > 8$ . **g)**  $C_s(\Delta)$  at  $s_5$  in both the experimental diffraction pattern (blue) and in the corresponding region of the SASA simulation (red). In panels **(d-g)** each  $C_s(\Delta)$  curve is fitted with a cosine function to provide a guide to the eye. **h)** Rendering of the hexagonal superlattice created by the sulfur atoms binding the ligands on the NPs surface. **i)** Rendering of the crystallographic planes created by carbon atoms chains of the dodecanethiol ligands. Carbon atoms on two facets of the NP are isolated for clarity.

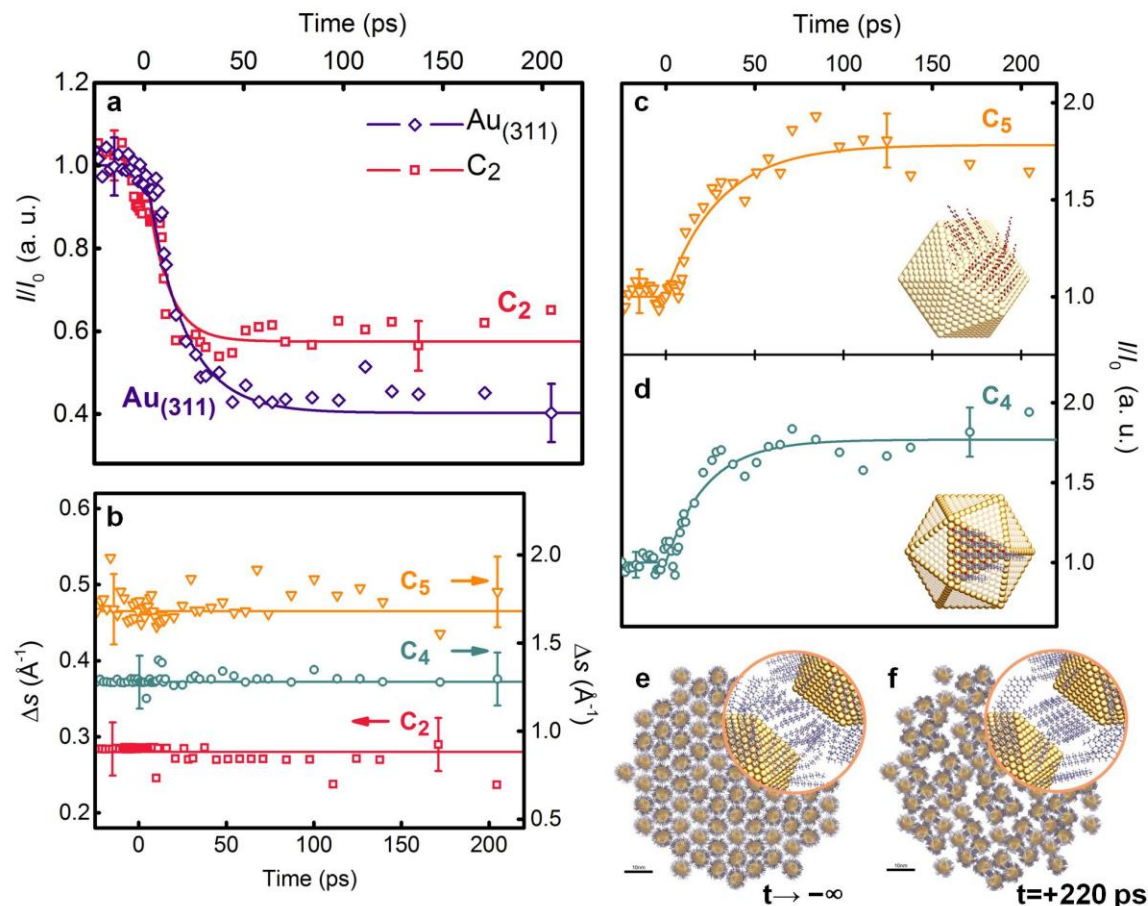


**Fig. 4. Small-angle ultrafast electron diffraction of dodecanethiol-capped NPs.** **a)** Dynamics of the intensity normalized to its value before  $t_0$  ( $I_0$ ) for the contrast peak  $C_2$  (red squares) and for the Debye-Scherrer ring corresponding to diffraction from the (311) crystallographic planes of the gold lattice in the NPs (blue rhombuses). **b)** Dynamics of the position for the contrast peaks  $C_2$  (red squares),  $C_4$  (green circles),  $C_5$  (orange triangles). The arrows indicate the related left or right vertical axis. **c)** Dynamics of the intensity normalized to its value before  $t_0$  ( $I_0$ ) for the contrast peaks  $C_5$  (orange triangles) and **d)**  $C_4$  (green circles). **e, f)** Frames from the computer-generated movie displaying the retrieved dynamics of a portion of the sample **e)** at equilibrium and **f)** at  $t = +220$  ps after light excitation. The recovery time for this sample exceeds the time-frame investigated in these experiments.

Contrast peak label	Position of the maximum, $s$ ( $\text{\AA}^{-1}$ )	Real space distances, $d = 2\pi/s$ ( $\text{\AA}$ )	Real space features
$C_0$	-	66.10	Crystallographic planes of the 2D supracrystal: $d_0$ (1 <sup>st</sup> order)
$C_1$	0.18	34.25	Crystallographic planes of the 2D supracrystal: $d_0$ , (2 <sup>nd</sup> order) and $d_1$ (1 <sup>st</sup> order)
$C_2$	0.27	22.83	Crystallographic planes of the 2D supracrystal: $d_0$ , (3 <sup>rd</sup> and 4 <sup>th</sup> order)
$C_3$	$s_3 = 0.55$	11.42	2 <sup>nd</sup> order of $C_2$
$C_4$	$s_4 = 1.26$	4.98	Superlattice of S atoms
$C_5$	$s_5 = 1.68$	3.72	Crystallographic-like arrangement of the carbon atoms in the ligands
$C_6$	$s_6 = 2.71$	2.31	Au <sub>(111)</sub> peak

**Table 1.** Positions of the contrast peaks with the corresponding real-space distances and real-space features of the system under observation.

## Supplementary Information:

### Sample preparation.

1-octanethiol, 1-dodecanethiol and 1-octadecanethiol-coated NPs were synthesized using a modification of the method described by Zheng *et al.*<sup>31, 32</sup>. A NPs monolayer was prepared by a drop-wise deposition of a toluene solution of NPs onto the water subphase of a Langmuir trough (for the case of 1-octadecanethiol-coated NPs the solution was kept at 30 °C until it was deposited to maintain the solubility). After 10 min the layer was compressed at 10 mm/min until it reached 18 mN/m (at the isotherm solid phase region) and then it was transferred to an amorphous carbon-coated grid through a Langmuir-Schaefer deposition. The TEM images of the three different supracrystals are reported in Fig. S1 (a-c); 1-octanethiol-coated gold NPs (Fig. S1 a) showed a core diameter of  $4.4 \pm 0.5$  nm and a core-to-core distance of  $6.0 \pm 0.6$  nm, while 1-octadecanethiol-coated gold NPs (Fig. S1 c) are characterized by a core diameter of  $4.8 \pm 0.3$  nm with a core-to-core distance of  $7.1 \pm 0.5$  nm.

The TEM image of the 1-dodecanthiol sample (Fig. 1a, main text), shows NPs arranged into a supracrystal, where the crystallographic planes and their corresponding distances  $d_0$  and  $d_1$  in the supracrystal are highlighted respectively in the upper and lower insets. In this TEM image, the ligands are not visible as they do not provide enough contrast for a 200 kV TEM. Some recent experiments demonstrated that the ligands may be observed at lower voltages<sup>33, 34</sup> but only for isolated particles.

### UED experimental setup.

Our set-up for Ultrafast Electron Diffraction and Femtosecond Electron Diffractive Imaging uses a KMLabs Wyvern Ti:sapphire amplified laser generating 50-fs (FWHM), 700- $\mu$ J pulses, centered at a wavelength of 800 nm and at a repetition-rate of 20 kHz. The temporal spread of the 30 kV probe electron pulses is controlled by means of a radiofrequency (RF) compression cavity<sup>35, 36</sup>, thus allowing to store up to  $6 \cdot 10^5$  electrons in  $\sim 300$  fs/160  $\mu$ m bunches at the sample<sup>18</sup>. The diffraction pattern is formed on a phosphor screen and is recorded by a charge-coupled device camera capable of single electron detection. The sample was oriented with respect to the probing electrons by a rotative sample holder with four degrees of freedom: three translations on  $x$ ,  $y$  and  $z$  axis and one rotation,  $\chi$ , around the  $z$  axis. Transmission experiments were performed at room temperature and with an almost collinear arrangement between the pump and probe pulses, in order to reduce the spatio-temporal mismatch between them. The background pressure in the experimental vacuum chamber was below  $10^{-9}$  mbar.

The diffraction pattern of the sample at equilibrium depicted in Fig. 1b (see main text) is the result of the stitching of two different experimental diffraction patterns. The separation between the two contributing diffraction patterns is marked in Fig. 1b by the black line at  $s=2.38 \text{ \AA}^{-1}$ .



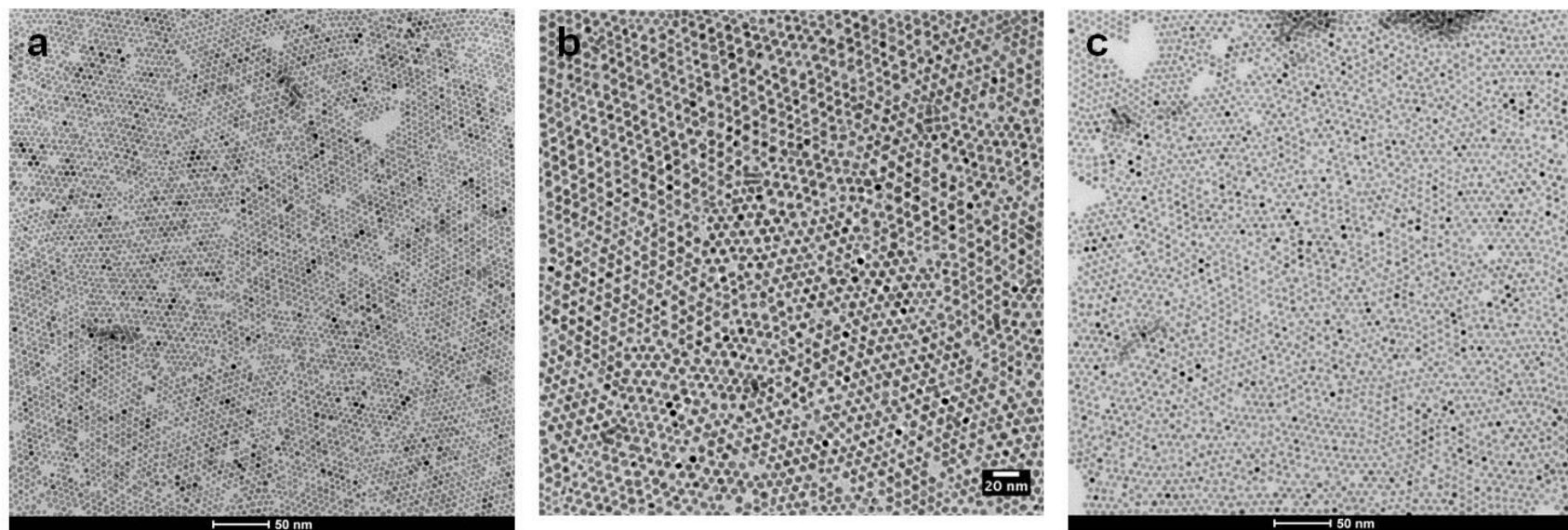


**Fig. S1.** TEM images of the supracrystals of (a) 1-octanethiol-coated gold NPs, (b) 1-dodecanethiol-coated gold NPs and (c) 1-octadecanethiol-coated gold NPs.

One diffraction pattern was recorded with a beam-block covering the direct electron beam up to a scattering vector value  $s=2.38 \text{ \AA}^{-1}$  to enhance the diffraction from the NPs gold cores.

The image is the result of averaging 50 frames containing  $5 \cdot 10^8$  electrons each for every time delay. The other diffraction pattern was acquired without beam stop by summing 740 images containing  $2 \cdot 10^5$  electrons each, and it spans the scattering vectors from  $s=0 \text{ \AA}^{-1}$  to  $s=2.38 \text{ \AA}^{-1}$  thus exhibiting the “small-angle” diffraction region. In the same figure the typical Debye-Scherrer rings of polycrystalline gold are found at high scattering vectors (large-angle diffraction region) and originate from the random orientation of the NPs in the supracrystal<sup>14</sup> probed by the electron beam of  $160 \text{ \mu m}$  spot-size. The radial averaged intensity is defined as:

$$I(s) = \frac{1}{2\pi} \int I(s, \theta) d\theta \quad (\text{S1})$$

and it is obtained by averaging the intensity  $I(s=\text{const}, \theta)$  over the azimuthal angle  $\theta$ .

One main advantage of these UED experiments is that the diffraction images are taken with a very small current (320.4 pC/s for every time delay, 4.11  $\mu\text{C}$  as total charge on the NPs with this amount being distributed over several electron pulses impinging on the sample), thanks to the use of a high sensitivity camera and the pulsed electron beam. Also, the very low duty cycle allows a large relaxation time between subsequent pulses. For these reasons, radiation damage is not observed in these experiments, as opposed to static TEM imaging experiments.

#### Simulation of the supracrystal of dodecanethiol-coated gold NPs: morphology and SASA simulated diffraction pattern.

Gold NPs cores have a polyhedral morphology, where the truncated-octahedral shape is predominant together with icosahedra, dodecahedra and decahedra. Small displacements from the bulk positions occur in the surface atomic layers near edges and vertices, resulting in a slight rounding of the gold core shape<sup>20</sup>. The shape of the gold core for our model was selected to be icosahedral as this is the most common shape which gold nanocrystals made of a few thousands of atoms have at equilibrium<sup>37, 38</sup>. We remark that the most important parameter for the SASA simulation is the arrangement of the gold atoms on the facets of the nanoparticle, which is more or less the same for different geometries of the core, as that arrangement defines the distribution of the ligands and their atoms. The gold atoms in our sample are arranged in a face-centered cubic (*fcc*) lattice, which is confirmed by the observed characteristic Debye-Scherrer rings in the diffraction pattern (see Fig. 2, main text): the radial averaged intensity profiles from the experimental diffraction (violet circles) and from the SASA simulation of the NPs gold cores (orange solid line) show a remarkable agreement. Furthermore for an *fcc* structure, the typical arrangements of atoms on facets is (111) surface, which is also the case for icosahedrally shaped nanostructures. For the above reasons the choice of a different model would not change the

speckle symmetry, or the position of the maxima, or the diffraction peaks arrangement. In fact, in the diffraction pattern, the peak positions are affected only by the distances between gold atoms, which are the same for any model chosen, whereas only the intensity distribution is defined by the shape of the nanocrystal. Although the choice of an exact model for the shape of gold NPs is an interesting study by itself, which involves a whole independent branch of research<sup>39, 40</sup>, we will not discuss it further as it goes beyond the scopes of the present study.

Dodecanethiol molecules bonded on the Au<sub>(111)</sub> facets of the NPs arrange preferably in the more thermodynamically stable *trans* isomers. *Trans* ligands among neighboring NPs interdigitate to compensate for the loss of density at the terminal part of the chains, while a minority of *gauche* chains occupy interstitial sites and domain boundaries<sup>21, 22, 41, 42</sup>. Furthermore, the faceted shape of the NPs core leads to the interlocking of molecular bundles (*i. e.* groups of ligands on each facet) on neighboring particles. The length of a dodecanethiol ligand completely stretched is 1.56 nm. In the all-*trans* conformation the molecule is tilted 30° from the surface normal; it is also twisted with respect to the molecular backbone by 55° and far from the nearest-neighbor by 14°<sup>(43)</sup>. These ligands are known to form a superlattice commensurate with the Au-Au (111) distance of the underlying NP facets. This hexagonal superlattice with 60° angles corresponds to a ligand-ligand spacing of 4.98 Å<sup>44</sup>.

A simulation of the NPs with ligands has been carried out taking into account for the above described parameters. Each gold core was created as an icosahedra and randomly rotated in 3D around the *x*, *y* and *z* axis. Dodecanethiol ligands were attached to the facets so that Au-S distance is 2.31 Å<sup>45</sup>. The ligands were randomly rotated around their axis. The simulation took into account the interlocking of molecular bundles on neighboring particles, the interdigitation of ligands belonging to different NPs and the interstitial folding of *trans* ligands on the same face of the same icosahedral NP core. *Trans* ligands were distributed on every NPs facet following the superlattice, while *gauche* isomers were placed at interstitial sites. A cluster of four NPs with different orientation was then assembled, as depicted in Fig. S2 a, and its electron diffraction pattern (Fig. S2 b) was calculated using the following parameters:

- Electron energy: 30 keV;
- Sample-detector distance: 230 mm;
- Sampling: 1000×1000 pixels;
- Pixel size in the detector plane: 50 μm.

Each atom was assigned its position in *x*, *y*, *z* coordinates and the complex-valued scattering amplitudes specific to each chemical element (Au, S, C, H) were calculated using the NIST library (NIST, electron elastic-scattering cross-section database 2000, NIST Standard Reference Database 71) for high-energy (30 keV) electrons. The complex-valued waves scattered off each atom were superimposed in the far-field and the intensity of the total wave field provides the diffraction pattern.

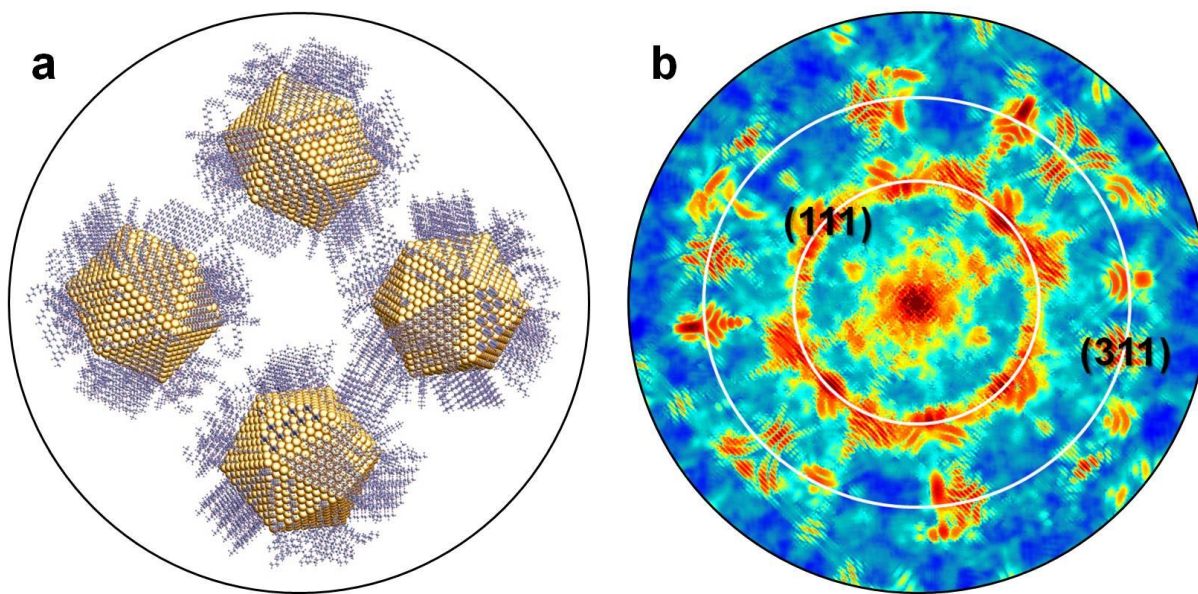


**Fig. S2.** Simulation of dodecanethiol-coated gold NPs. **a)** Four randomly rotated NPs. **b)** Corresponding simulated diffraction pattern obtained by superposition of atomic scattering amplitudes (SASA).

#### Spheres Lattice Model (SLM) simulations.

The Spheres Lattice Model (SLM) was created to mimic the distribution of the NPs in the supracrystal from being ideally ordered into a triangular lattice to disordered, and to compare its diffraction pattern to the FT of the TEM image. The NPs in the SLM are represented as ideal spheres. The model uses two parameters: the diameter of the spheres and the distance between them. In order to introduce disorder into a perfectly ordered spheres distribution, the following routine has been designed. Starting from the perfectly arranged two-dimensional lattice of spheres (Fig. S3 a), the program selects round domains and rotates them by the angle  $\eta$ , where  $\eta$  is Gaussian distributed with the mean=0 and standard deviation  $\sigma$ . The domains are selected to have a size of 60 nm and a centre-to-centre distance between domains of 80 nm. Two simulated spheres distributions for  $\sigma = 20^\circ$  are shown in Fig. S3 (b, c). Figure S3 b shows the result from the simulation for  $\sigma = 20^\circ$ , with a perfectly ordered spheres arrangement preserved within each domain. In a following step, the disorder of individual NPs positions was introduced by adding a random shift up to  $\Delta r = \pm 1$  nm for each NP (Fig. S3 c).

The best agreement between the FT of the SLM simulations and the FT of the TEM image was found for the following spheres parameters: core-to-core distance of 7.63 nm and gold-core diameter of 5.70 nm. The right panel of Fig. S3 shows the radial averaged intensity ( $I(s)$ ) of the FT of the TEM image (Fig. S3 d, purple curve), compared to that of the FTs from the three different SLM simulations (Fig. S3 (a-c)).

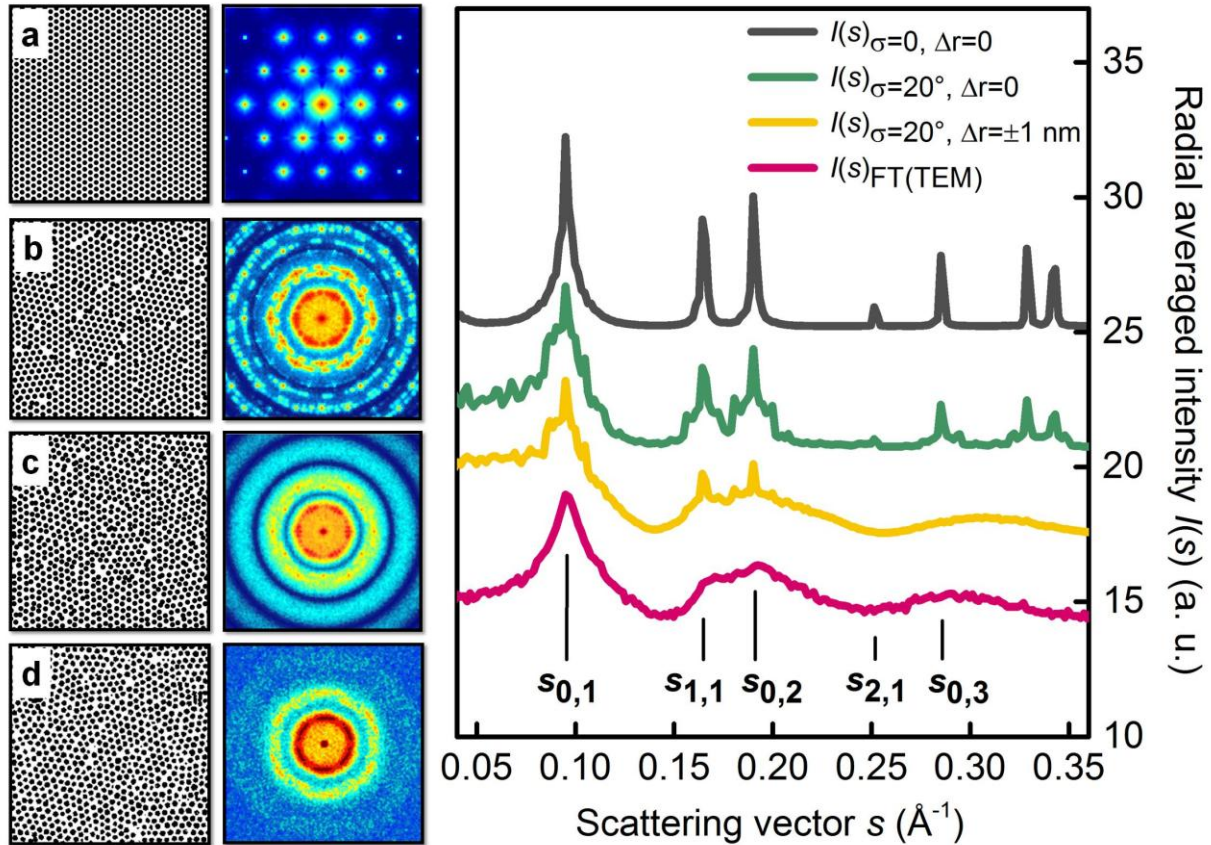


**Fig. S3.** Simulations of the 2D supracrystal of gold NPs with different degrees of disorder. Left panel: **a-c**) Simulated distribution of spheres (SLM model) and corresponding simulated diffraction patterns (FTs). In particular: **(a)** Perfectly arranged spheres, **(b)** Lattice with domains rotated with  $\sigma=20^\circ$  and **(c)** the same as **(b)** but with each NP shifted around its position by  $\pm 1$  nm. **d**) TEM image of the sample under investigation and corresponding FT. Right panel: Related radial averaged intensity  $I(s)$  curves for the perfect lattice (grey curve), the SLM simulation with  $\sigma = 20^\circ$  and  $\Delta r = 0$  (green), the SLM simulation with  $\sigma = 20^\circ$  and  $\Delta r = \pm 1$  nm (yellow) and the experimental FT of the TEM image (purple).

The perfect ordering of the spheres leads to pronounced peaks in the simulated diffraction pattern (Fig. S3 a) and hence in the radial averaged intensity (grey curve). These same diffraction features are found in the  $I(s)$  from the FT of the TEM image, as indicated in both Fig. 2 (see main text) and in the right panel of Fig. S3. The best agreement between  $I(s)$  from the FT of the SLM simulations and the FT of the TEM image is observed for the SLM model with  $\sigma=20^\circ$  and the random shift of the NPs positions up to 1 nm (Fig. S3 c), where the yellow color is for the simulation and the purple color is for the FT of the TEM image.

Figure S3 shows schematically how the diffraction pattern changes upon increasing disorder in the system. The FT of the SLM simulation for a perfectly ordered lattice consists of sharp peaks



(Fig. S3 a). Upon introducing randomization in the form of domain-like distribution of NPs, by setting  $\sigma = 20^\circ$ ,  $\Delta r = 0$  in the SLM simulation, the sharp peaks smear out (Fig. S3 b). When the additional shift of up to  $\Delta r = \pm 1$  nm is introduced in the NPs positions, the sharp peaks in the diffraction pattern disappear and Debye-Scherrer rings dominate the pattern (Fig. S3 c). Note the matching between the simulated (Fig. S3 c) and the experimental (Fig. S3 d) diffraction patterns. Thus, the arrangement of spheres with  $\sigma = 20^\circ$  and  $\Delta r = \pm 1$  nm models well our sample and represents the typical signature of a colloidal system. In this frame, what appears to be a randomized disordered system still contains hidden information on local symmetries which can be retrieved through the computation of the angular normalized intensity and angular cross-correlations (see main text).

The SLM model is designed to match the arrangement of the NPs to that in TEM image of the sample. In both images, SLM and TEM, NPs are represented as opaque objects. Strictly speaking, NPs do not behave as opaque objects when interacting with electron waves. However, for the purpose of matching the NPs arrangement in the SLM and the TEM images by comparing their Fourier transforms, the phase distribution of the NPs can be neglected. Should one introduce phase-shifting properties of the NPs, it must be done in the same manner for both, SLM and TEM image, which apparently will cause the same effect in their Fourier transforms. For smaller length scale, where the positions of individual atoms play a role, the results of SASA simulations are employed, which take into account three-dimensional positions of each atom and the related phase shifts.

### Speckle pattern analysis.

Systems lacking a defined translational symmetry can still exhibit characteristic peaks in diffraction pattern, provided the disordered sample contains locally ordered regions. These ordered regions can be randomly distributed throughout the sample, and they create specific peaks in the diffraction pattern, provided that the incident radiation has a spatial coherence length at least comparable to the size of these ordered sub-volumes<sup>46</sup>.

The speckle pattern represents a unique fingerprint of the sample in real space. The analysis of the speckle pattern intensity dynamics as a function of time allows reconstructing a stroboscopic movie of the sample upon photo-excitation. Diffraction from a sample of disordered identical particles, observed with waves of limited coherence, typically results in Debye-Scherrer rings. It has been demonstrated that the angular cross-correlation of the intensity along a ring in the diffraction pattern from a colloidal sample exhibits certain modulations, which can be tracked back to the local symmetry of the scattering object (see main text)<sup>23, 24</sup>. The coherence length of our system allowed us recording the diffraction pattern where the modulations in the speckle were detected directly from azimuthal intensity distribution.

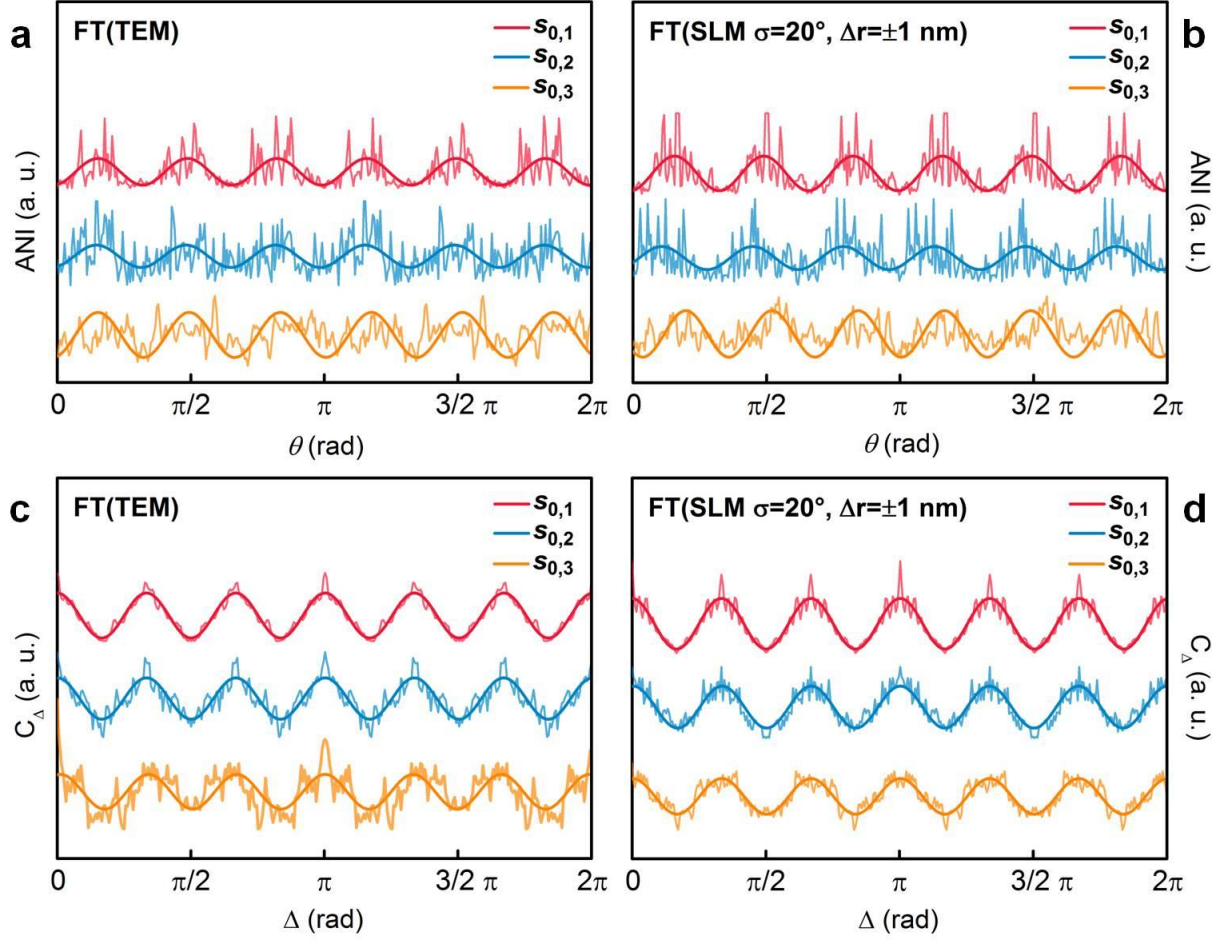


**Fig. S4.** Comparison of ANI and  $C_s(\Delta)$  for the first three orders of  $s_0$ :  $s_{0,1}$ (red),  $s_{0,2}$ (blue),  $s_{0,3}$ (orange). **a, c)** Results from the FT of the TEM image. **b, d)** Results from the FT of the SLM ( $\sigma=20^\circ$ ,  $\Delta r = \pm 1$  nm) simulation of the supracrystal.

Symbol	Scattering vector $s$ ( $\text{\AA}^{-1}$ )	Real-space distances $d = 2\pi/s$ (nm)
$s_{0,1}$	0.095	6.61
$s_{1,1}$	0.165	3.82
$s_{0,2}$	0.190	6.61
$s_{2,1}$	0.274	2.29
$s_{0,3}$	0.285	6.61

**Table S1:** Diffraction orders from the crystallographic arrangement of NPs in the supracrystal.

### Diffraction from crystallographic arrangement of NPs in the supracrystal, angular intensity and angular cross-correlation at $s_0$ .

The diffraction orders from the crystallographic arrangement of NPs in the supracrystal are summarized in Table S1. The lowest order of diffraction comes from  $d_0$ . The crystallographic planes with distances  $d_0=6.61$  nm and  $d_1=3.82$  nm are depicted in the inset of Fig. 1a (see main text). The  $C_s(\Delta)$  ( $s=s_{0,3}$ ) in the experimental diffraction pattern and in the FT of the TEM image exhibits a six-fold distribution, as depicted in Fig. 3d (see the main text). The lower orders of  $s_0$

( $s_{0,n} = n \cdot \frac{2\pi}{d_0}$  with  $n=1, 2$ ), related to the crystallographic planes with distance  $d_0= 6.61$  nm,

show the same periodicity as  $s_{0,3}$ . This is confirmed by the ANI and the angular cross-correlation profiles of the FT of the TEM image (Fig. S4 a, c) and in the ones from the FT of the SLM model with  $\sigma =20^\circ$  and  $\Delta r = \pm 1$  nm (Fig. S4 b, d).

### Simulation of the structure diffracting at $s_5$ peak.

Our simulation allowed us to separate the diffracted waves from different atoms. For a single NP, atoms of the same chemical type were separated and their three-dimensional (3D) distribution  $D(x,y,z)$  was considered. The 3D reciprocal distribution was obtained by calculating the 3D Fourier transform of the carbon atoms positions  $I(k_x,k_y,k_z)$ , see Fig. S5. A diffraction pattern is then obtained as an intersection of the  $I(k_x,k_y,k_z)$  distribution with the Ewald sphere (shown in green) that goes through the center of  $I(k_x,k_y,k_z)$ . Diffraction only occurs when a reciprocal lattice point lies on the Ewald sphere. As the radius of the Ewald sphere is very large, it is in fact an intersection of the  $I(k_x,k_y,k_z)$  distribution with the plane which goes through the center of  $I(k_x,k_y,k_z)$ . The diffraction patterns from all the possible orientations of a NP can be obtained by rotating the reciprocal 3D lattice  $I(k_x,k_y,k_z)$  and keeping unchanged the direction of the incident probing beam.

The intensity at the position of the peak  $s_5$  has then been studied; it was found that the diffraction at  $s_5$  occurs only when carbon atoms were considered. Next, it was found that on the sphere of radius  $s_5$  (shown in red) only six diffraction spots were observed. Thus, by careful selection of the direction of the incident wave only two diffraction spots can be observed in the diffraction pattern. These originate from the diffraction on the carbon atoms that belong to a bunch of well-ordered ligands on one facet of the NP. When two such groups of carbon atoms from two different facets are added, the intensity distribution shows four intense peaks. Thus, the diffraction pattern with four peaks at  $s_5$  is actually a combination of two two-fold centrosymmetrical diffraction patterns generated by two sets of aligned ligands, as depicted by the rendering of Fig. 3i (see main text). The two sets of aligned ligands represent the locally ordered region in the sample which is randomly distributed on a single NP surface and throughout the entire supracrystal.



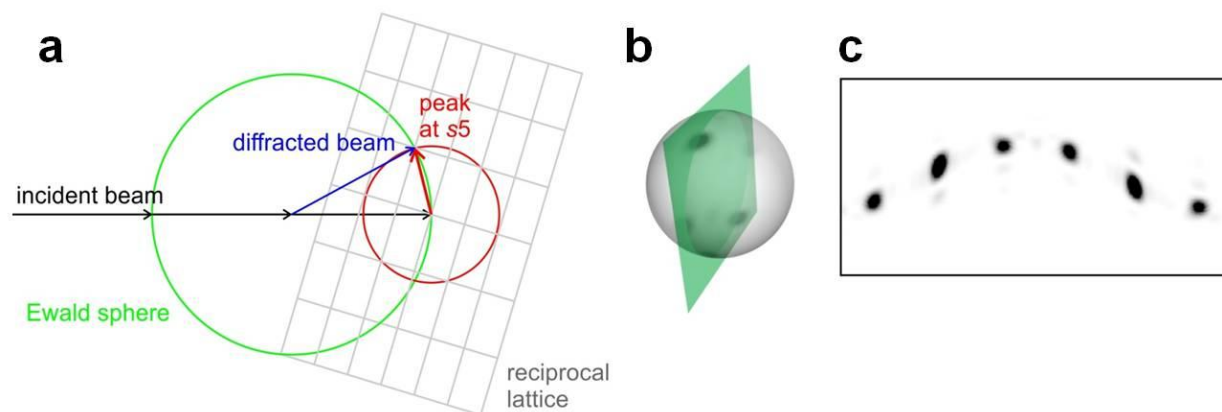


**Fig. S5.** Formation of the diffraction pattern as an intersection of the reciprocal lattice with the Ewald sphere. **a)** Illustration to the Ewald sphere. **b)** 3D representation of intersection of the Ewald sphere with the reciprocal lattice at radius  $s_5$ , when only carbon atoms are considered. The sub-sphere corresponds to the red circle in **a**. **c)** Distribution of the reciprocal lattice on the sub-sphere of radius  $s_5$  shown in **b**.

The random distribution of this locally ordered “base-unit” generates the four-fold speckle pattern at  $s_5$  that we are able to detect in UED and whose symmetry can be investigated through the computation of the ANI and  $C_s(\Delta)$  profiles (see Fig. 3g, main text). The dynamics of its corresponding contrast peak  $C_5$  unravels information on how this base unit evolves in the sample as a response to the 1.5 eV optical excitation.

#### Movie.

In the supplementary information we present a computer-generated movie (“Movie S1.wmv”) showing the disordering and ordering dynamics of the supracrystal upon ultrafast laser excitation. The photo-excitation causes thermal disorder in the gold cores ( $18 \pm 3$  ps) and the supracrystal ( $11 \pm 3$  ps). Inset: the motion of the NPs causes the stretching of the ligands, which takes place with a slower dynamics ( $30 \pm 4$  ps). In the rendering we reduced the number of ligands on the NPs gold core facets, with respect to the SASA model, for clarity.